

Cite this: *Biomater. Sci.*, 2024, **12**, 748

Oxygen and pH responsive theragnostic liposomes for early-stage diagnosis and photothermal therapy of solid tumours†

Siyi Li,^a Qinglin Wang,^a Yingying Ren,^a Pengfei Zhong,^{b,c} Pengtao Bao,^c Shanyue Guan,^{*d} Xiaochen Qiu^{*e} and Xiaozhong Qu  ^{*a,f}

The development of cancer treatment is of great importance, especially in the early stage. In this work, we synthesized a pH-sensitive amphiphilic ruthenium complex containing two alkyl chains and two PEG chains, which was utilized as an oxygen sensitive fluorescent probe for co-assembly with lipids to harvest a liposomal delivery system (RuPC) for the encapsulation of a photothermal agent indocyanine green (ICG). The resultant ICG encapsulated liposome (RuPC@ICG) enabled the delivery of ICG into cells *via* a membrane fusion pathway, by which the ruthenium complex was localized in the cell membrane for better detection of the extracellular oxygen concentration. Such characteristics allowed ratiometric imaging to distinguish the tumour location from normal tissues just 3 days after cancer cells were implanted, by monitoring the hypoxia condition and tracing the metabolism. Moreover, the pH sensitivity of the liposomes favoured cell uptake, and improved the anti-tumour efficiency of the formulation *in vivo* under NIR irradiation. Assuming liposomal systems have fewer safety issues, our work not only provides a facile method for the construction of a theragnostic system by combining phototherapy with photoluminescence imaging, but hopefully paves the way for clinical translation from bench to bedside.

Received 18th September 2023,
Accepted 5th December 2023

DOI: 10.1039/d3bm01514a

rsc.li/biomaterials-science

Introduction

The early screening of solid tumours can greatly improve the survival of cancer patients,¹ and rapid medical diagnosis is critical.² Accurate diagnosis of the location of early-stage tumours relies on probes that are highly sensitive to the tumour micro-environment.^{3,4} Traditional cancer screening methods include imaging screening such as ultrasound, computed tomography (CT), magnetic resonance imaging (MRI), and endoscopic screening like gastroscopy and colonoscopy,⁵ as well as the combination of two or more complementary

modalities to achieve so called correlative multimodal imaging (CMI) that creates composite and complementary views of the sample.⁶ Recently, fluorescence probing methodologies, for example using excitation by visible and near-infrared (NIR) light, have demonstrated advantages of high spatial and temporal resolution, good sensitivity, and *in situ* visualization for precise early diagnosis.⁷ Although the penetration depth of light in tissues might be a limitation, the optical method can be very sensitive to detect superficial tumours. The resolution of tumour imaging normally depends on the accumulation and emission characteristics of the fluorophore at the tumour site.⁸ Therefore the development of tumour-associated, stimulus-driven, deep-penetration and turn-on photosensitizers are attracting increasing attention for selective and precise tumour diagnosis.^{7,9–11} Nonetheless, it is also noted that even with the inclusion of targeting agents, the broad biodistribution of fluorescent probes may not be avoided following systemic administration, especially when the tumour growth is incipient.^{12,13} Distinguishing the tumour specific signal from comprehensive optical signals is thus necessary.

Hypoxia is a well-known hallmark of the tumour microenvironment, originating from anaerobic glycolysis due to the rapid proliferation of tumour cells,^{14,15} which also results in the decrease of the extracellular pH (pH_e) in tumour tissue following the metabolism of glucose.¹⁶ Therefore, oxygen and pH

^aCenter of Materials Science and Optoelectronics Engineering, College of Materials Science and Opto-Electronic Technology, University of Chinese Academy of Sciences, Beijing 101408, China. E-mail: quxz@ucas.ac.cn

^bHebei North University, Hebei 075000, China

^cThe Eighth Medical Center, Chinese PLA General Hospital, Beijing 100094, China

^dKey Laboratory of Photochemical Conversion and Optoelectronic Materials, Technical Institute of Physics and Chemistry, Chinese Academy of Sciences, Beijing 100190, China. E-mail: guanshanyue@mail.ipc.ac.cn

^eDepartment of General Surgery, the First Medical Center of Chinese PLA General Hospital, Beijing 100853, China. E-mail: qiuxiaochen1987@163.com

^fBinzhou Institute of Technology, Weiqiao-UCAS Science and Technology Park, Shandong 256606, China

† Electronic supplementary information (ESI) available: Supplementary figures. See DOI: <https://doi.org/10.1039/d3bm01514a>



sensitive systems have been investigated for tumour diagnostics and tumour-specific drug delivery.^{17–20} In particular, various kinds of platinum, iridium and ruthenium(II) complexes have been synthesized as oxygen probes for the visualization of tumour sites in animal models, under the mechanism of oxygen quenching.^{21–24} However, under the steady-state measurement of emission intensity, the accuracy of tumour identification will always be affected by the biodistribution of the probe because the concentration of fluorescent molecules also affects the emission strength.²⁵ Ratiometric imaging by the combination of sensitive and unresponsive probes could overcome the problem,^{25,26} and previously we have developed a dual-probe system containing both an oxygen sensitive ruthenium complex and oxygen insensitive Cy5.5, which has allowed us to quantitatively image the oxygen distribution in the brain tissue of living animals.²⁷ The ratiometric method is thus expected to help to distinguish the tumour location from normal tissue.

Theranostics is of importance for tumour therapy.²⁸ The co-delivery of therapeutic agents together with diagnostic probes is a requirement for drug carriers. For instance, some ruthenium complexes can generate reactive oxygen species (ROS) or singlet oxygen species (¹O₂), and therefore ruthenium complex loaded monolayer layered double hydroxide (LDH) was fabricated with the convertible properties of two-photon fluorescence imaging and singlet oxygen generation, switched by alternating the excitation wavelength.^{27,29} In another work, an oxygen insensitive upconversion probe of carbon dots (CDs) was coupled with oxygen sensitive ruthenium complexes (Ru₂b) for the synthesis of hypoxia responsive nanosensors to monitor the *in vivo* hypoxia status at tumour sites.³⁰ Nevertheless, in some cases, the delivery of therapeutic and diagnostic molecules may target different destinations. For example, while photodynamic and photothermal agents prefer an intracellular distribution for killing tumour cells,^{31,32} oxygen and pH imaging should reflect the extracellular micro-environmental conditions of the tumour tissue.¹⁵ Additionally, the premature release of probes in the extracellular matrix could lead to poor preservation of the fluorophores in tumour tissue since they could be diluted away by body fluid or diffuse in the cells under a rapid process.^{17,33} Therefore, research on theragnostic formulations with managed transportation of diagnostic and therapeutic agents is desired.

Current drug delivery pathways include endocytosis, phagocytosis, intermembrane transfer, membrane fusion, *etc.*³⁴ Comparably, membrane fusion is less energy intensive.³⁵ Direct intracytoplasmic delivery is able to send 100% of the packaged cargo into the cytoplasm.³⁴ Moreover, membrane fusion can transfer substances directly to the cell membrane in addition to the interior of the cell, which may allow the delivery of sensing and therapeutic photosensitizers to the cell membrane and cytoplasm respectively, and hence improve their functionalities for detecting the extracellular environment and generating heat to cause cell apoptosis under a suitable excitation wavelength.^{36,37} Liposomes are such a nano-system that can encapsulate material in both the lipid-formed

bilayer and the hydrophilic cavity,³⁸ with an internalization pathway that can be controlled to follow a membrane fusion process, owing to the structural similarity of the liposome membrane and cell membrane.^{34,39} Commonly, hydrophobic and amphiphilic molecules favourably locate in the lipid layer of liposomes,^{38,40} which are anticipated to fuse into the membrane of the targeted cell, while hydrophilic molecules tend to locate in the internal aqueous phase. Meanwhile, the oxygen sensing moieties like a ruthenium complex are hydrophilic.²² Therefore, to accurately transport and stably mount a fluorescent probe in the cell membrane becomes a key issue to apply liposomal carriers to tumour theragnostics.

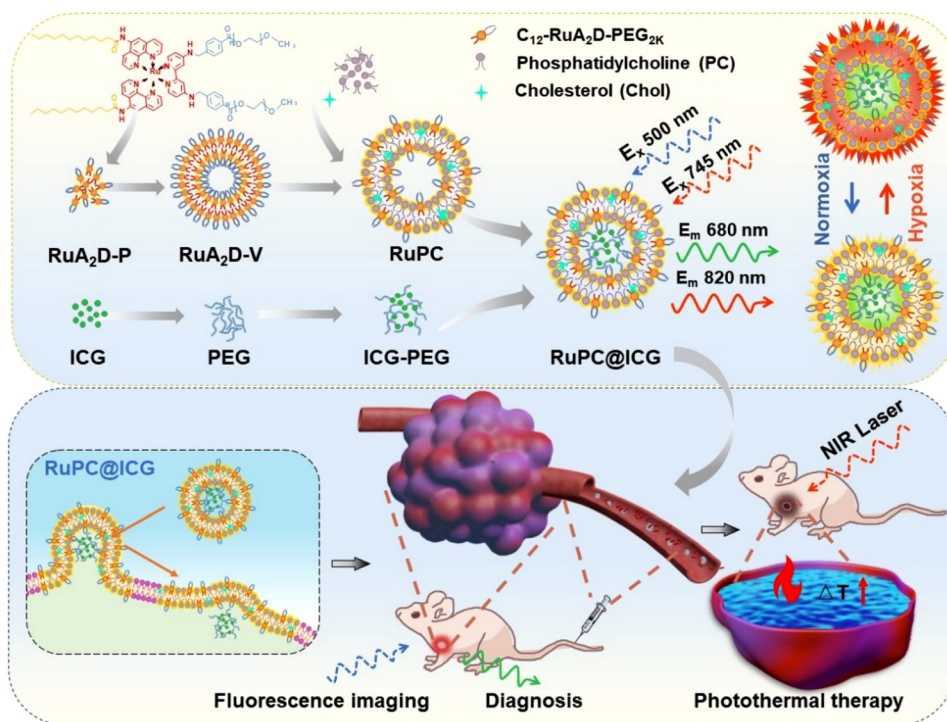
In this work, a ruthenium complex, *i.e.* RuA₂D, was synthesized and subsequently modified with two alkyl chains to obtain an amphiphilic probe, *i.e.* C_{*n*}-RuA₂D, for co-assembly with phosphatidylcholine (PC). The amphiphilicity of the RuA₂D molecule was further adjusted by PEGylation using benzaldehyde capped poly(ethylene glycol) methyl ether (mPEG) through the formation of a tumour pH_c sensitive acid-labile benzoic-imine linkage.^{41–43} Liposomes composed of the amphiphilic pH sensitive ruthenium complex (C_{*n*}-RuA₂D-PEG) and PC were then prepared to encapsulate indocyanine green (ICG), which is a clinically available NIR photosensitizer for photothermal therapy (PTT), to harvest a vesicular theragnostic formulation, namely, RuPC@ICG. We expected that RuPC@ICG can fuse onto the cell membrane for improved hypoxia sensing of the extracellular environment and meanwhile deliver the PTT agent into the cytoplasm for enhancing the efficiency. While the pH sensitivity of the liposome would accelerate its accumulation in tumour tissue, the co-delivery of ICG also provided a reference dye, in addition to the role of PTT agent, for achieving ratiometric imaging with the ruthenium complex in order to improve the recognition of the tumour site. This paper focuses on the investigation of the interaction between the RuPC@ICG liposome and tumour cells, as well as the synergistic ability of the formulation for the early detection and PTT therapy of solid tumours in an animal model (Scheme 1).

Experimental

Materials

1,10-Phenanthroline-5-amine, lauric acid, *n*-octanoic acid, and octanoic acid were purchased from Aladdin Co., Ltd (China). *N,N'*-dicyclohexylcarbodiimide (DCC), 4-dimethylaminopyridine (DMAP), *N*-hydroxysuccinimide (NHS) and 1-(3-(dimethylamino)propyl)-3-ethylcarbodiimide hydrochloride (EDC) were purchased from J&K Chemical Ltd. 4-*p*-Carboxybenzaldehyde (4-CBA), methoxy poly(ethylene glycol) (mPEG) (*M*_w = 1000 Da, 2000 Da and 5000 Da), methoxy poly(ethylene glycol) amine (*M*_w = 2000 Da), phosphatidylcholine (PC) and cholesterol (CHOL) were obtained from Shanghai McLean Biochemical Technology Co., Ltd. [(*p*-Cymene)RuCl₂]₂, 4,4'-diamino-2,2'-bipyridine were acquired from Beijing RHAWN Reagent Co., Ltd. Mono-sulfo-cy7.5 NHS (ICG-NHS)





Scheme 1 Schematic illustration of the preparation process of oxygen and pH sensitive liposomal carriers to encapsulate a photosensitizer (RuPC@ICG) as a theragnostic agent to deliver the photosensitizer into cells through a membrane fusion pathway, and meanwhile mount the oxygen sensor in the cell membrane for detecting the tumour hypoxia condition, and later on photothermal therapy on the tumour site.

was bought from Shaanxi Xinyan Bomei Biotechnology Co., Ltd. Dulbecco's modified Eagle's medium (DMEM), phosphate-buffered saline (PBS) and 0.25% Trypsin-EDTA were obtained from Gibco (Grant Island, U.S.A.). Fetal bovine serum (FBS) and penicillin-streptomycin solution were purchased from Solarbio (Beijing, China). Solvents and other compounds were purchased from Beijing Chemical Reagents Company (China) and used without further purification.

Characterizations

Fourier transform infrared spectra (FTIR) were recorded on a Bruker Vertex70 spectrophotometer in the range 4000–400 cm^{-1} with 2 cm^{-1} resolution. Nuclear magnetic resonance (^1H NMR) spectra were recorded on a Bruker AVANCE III HD spectrometer. MALDI-TOF-MS was carried out using a Bruker BIFLEX III mass spectrometer. Zeta potential measurement and dynamic light scattering (DLS) were performed on a MALVERN Mastersizer 2000. The morphology was observed using transmission electron microscopy (Hitachi HT7700 Exalens, Japan). Electron spin resonance (ESR) spectra were plotted using a Bruker 500 spectrometer. Laser confocal scanning microscopy (LCSM) was performed on a Leica STELLARIS.

Synthesis of alkyl chain modified phenanthroline

1,10-Phenanthroline-5-amine (357 mg, 1.83 mmol), lauric acid (400 mg, 2 mmol), EDC (882 mg, 4.6 mmol) and DMAP (223 mg, 1.83 mmol) were dissolved in 50 mL of dichloro-

methane (DCM) and reacted for 1 h at 4 °C and then 48 h at 30 °C to obtain a light-yellow solution. The solvent was removed by rotary evaporation under reduced pressure, and 100 mL of deionized water was added. The dispersion was filtered through ordinary filter paper after ultrasonic dispersion to obtain a milky white filter residue. The above filtration operation was repeated three times, and the final product was dried under vacuum to obtain the white solid powder C_{12} -grafted phenanthroline (485 mg) with a yield of 67% (Fig. S1†). For MALDI-TOF, $m/z = 378.385$ (calcd 377.25). C_8 - and C_{18} -grafted phenanthroline were also prepared in the same way, but using *n*-octanoic acid and octadecanoic acid, respectively. The chemical structure was characterized using FTIR and ^1H NMR (Fig. S2†).

Synthesis of mPEG with a benzaldehyde end group (mPEG_{2K}-CHO)

mPEG_{2K} ($M_w = 2000$ Da, 4.0 g, 2 mmol), 4-CBA (2.4 g, 16 mmol), DCC (3.3 g, 16 mmol) and DMAP (122 mg, 1 mmol) were added to 60 mL of DCM, sonicated for 10 min, and then stirred at 37 °C for 24 h. The insoluble solid *N,N*-dicyclohexylurea (DCU) was removed by filtration. The solvent in the filtrate was evaporated to obtain a pale-yellow residue. To this, 50 mL of isopropyl alcohol (IPA) was added and the mixture was heated to 70 °C. The solution was then recrystallized at –20 °C for 24 h, and the resulting crystal was obtained by centrifugation, washed using IPA three times and dried under vacuum to give a white powdered product mPEG_{2K}-CHO



(4.9 g) with a yield of 77% (Fig. S1†). mPEG_{1K}-CHO and mPEG_{5K}-CHO were prepared using mPEG_{1K} and mPEG_{5K} in the same way. The structures were characterized by FTIR and ¹H NMR (Fig. S2†).^{40,41}

Synthesis of amphiphilic ruthenium complex (C_n-RuA₂D-PEG)

The reagents, [(*p*-cymene)RuCl₂]₂ (90 mg, 150 μmol) and 4,4'-diamino-2,2'-bipyridine ligand (55 mg, 300 μmol), were dissolved in 20 mL of ethanol. The solution was bubbled with nitrogen to remove oxygen for 30 min, and then reacted at 35 °C for 4 h to obtain a brownish yellow solution. Then C₁₂-grafted phenanthroline (225 mg, 223 μmol) was added to the reaction solution, and refluxed at 80 °C for 12 h. The solvent was removed by spin evaporation, and 20 mL of acetone was added and stirred at room temperature for 6 h. Then the brownish red filter residue, *i.e.* the C₁₂-RuA₂D product, was obtained by filtration in 76.3% yield (233 mg) (Fig. S1†). For MALDI-TOF-MS, *m/z* = 1041.686 (calcd 1042.49). C₈-RuA₂D and C₁₈-RuA₂D were also synthesized in the same way, and the chemical structure was characterized by FTIR and ¹H NMR as shown in Fig. S2.†

C₁₂-RuA₂D (32 mg, 32 μmol) was then dissolved in 15 mL of methyl alcohol, to which mPEG_{2K}-CHO (260 mg, 129 μmol) was added and stirred at 25 °C for 24 h. The mixture was filtered and the filtrate was concentrated to 2 mL for passing through a Sephadex LH-20 column with methyl alcohol as the eluent to remove unreacted PEG to get PEGylated C₁₂-RuA₂D, *i.e.* C₁₂-RuA₂D-PEG_{2K} (Fig. S1†). By changing the reagents, C₈-RuA₂D-PEG_{1K}, C₁₂-RuA₂D-PEG_{1K}, C₁₂-RuA₂D-PEG_{5K} and C₁₈-RuA₂D-PEG_{5K} were also synthesized. The products were then characterized using FTIR and ¹H NMR (Fig. S2†).

Synthesis of PEGylated ICG (ICG-PEG)

mPEG-NH₂ (7.25 mg, 3.6 μmol, *M_w* = 2000 Da) and ICG-NHS (1 mg, 1.2 μmol) were added to a mixed solvent containing 1 mL of DCM and 5 mL of PBS (pH = 7.4, 0.02 M) for stirring at 25 °C for 12 h. After removing DCM, the samples were dialyzed in a dialysis bag with a molecular weight cut-off of 2000 Da for 24 h and then lyophilized. The structure of the product was characterized by ¹H NMR and FTIR (Fig. S2†).

Synthesis of ICG-PEG encapsulated co-assembled liposomes of C_n-RuA₂D-PEG and phosphatidylcholine (RuPC@ICG)

First, 10 mg of C₁₂-RuA₂D-PEG_{2K}, 5 mg of PC, and 0.5 mg of CHOL in 10 mL of trichloromethane were mixed and put in a shaking incubator for 120 min (25 °C, 200 rpm). The solvent was then removed by spin evaporation under reduced pressure, and ICG-PEG (2 mg) was added in 2 mL of PBS (pH = 7.4). After sonication for 10 min, the dispersion was put into the shaking incubator again and shaken for more than 120 min (25 °C, 200 rpm), and then dialyzed against 1.5 L of PBS to obtain an ICG-PEG encapsulated co-assembly of C₁₂-RuA₂D-PEG_{2K} and PC (RuPC@ICG). In addition, empty co-assembled RuPC liposomes without the encapsulation of ICG were also prepared following the solvent evaporation procedure.

Self-assembled RuA₂D vesicles (RuA₂D-V) were prepared by dissolving 10 mg of C₁₂-RuA₂D-PEG_{2K} in 10 mL of trichloromethane. The mixture was placed in a shaking incubator for 120 min (25 °C, 200 rpm), and the solvent was removed by rotary evaporation under reduced pressure, followed by the addition of 2 mL of PBS (pH = 7.4). Rough particulate dispersions of C₁₂-RuA₂D-PEG_{2K} (RuA₂D-P) and ICG-PEG were prepared as control samples by directly sonicating C₁₂-RuA₂D-PEG_{2K} or ICG-PEG in PBS.

Oxygen sensitivity of RuPC@ICG

To determine the oxygen responsiveness of the RuPC@ICG, 2 mL of the dispersed sample was pipetted into a quartz cuvette, and bubbled by a mixed gas of O₂ and N₂ at different fractions with a flow rate of 600 mL min⁻¹. After balancing for 10 min, the fluorescence spectra were measured using an FL970 fluorescence spectrophotometer.

Photothermal effect of ICG formulations

First, 1 mL of RuA₂D-P, ICG-PEG and RuPC@ICG dispersed in PBS were irradiated under an 808 nm laser with an optical power density of 1 W cm⁻² for 10 min to study the photothermal profiles, with pure PBS as a negative control. In addition, the concentration-dependent photothermal effect of RuPC@ICG was examined by irradiating its dispersion at 50, 100, 200, and 500 μg mL⁻¹. The effects of the power density were investigated by changing the laser power to 0.25, 0.5, 0.75, 1.0 and 1.5 W cm⁻². The photothermal stability of the RuPC@ICG solution (200 μg mL⁻¹) was investigated by exposing and shielding the sample under an 808 nm laser (1 W cm⁻²) for five cycles. The temperature of the sample dispersions was captured by a thermal infrared camera.

Reactive oxygen species (ROS) scavenging

The triple peak (1 : 1 : 1) of single linear oxygen was captured using 2,2,6,6-tetramethyl-4-piperidone (TEMP) as a spin trapping agent utilizing electron spin resonance (ESR) spectroscopy to characterize the ROS generated by PBS, RuA₂D-P, ICG-PEG and RuPC@ICG. The generation of ¹O₂ was confirmed by the enhancement of the ESR signal generated by the reaction of TEMP with ¹O₂ as the irradiation time was increased from 0 to 10 min.

Cell culture

HeLa cervical adenocarcinoma cells were cultured in DMEM medium supplemented with 10% fetal bovine serum (FBS) and 1% penicillin-streptomycin for proliferation. Cells were cultured at 37 °C in a humidified atmosphere containing 5% CO₂.

Cytotoxicity measurements

The *in vitro* cytotoxicities of RuA₂D-P, ICG-PEG and RuPC@ICG were assessed on HeLa cells. The cells were first incubated in 25 cm² cell culture flasks and then inoculated into 96-well plates (1 × 10⁴ cells per well). After inoculation, the cells were exposed to a series of doses of the samples (C₁₂-



RuA₂D-PEG_{2K}: 31, 63, 125, 250, 500, 1000 $\mu\text{g mL}^{-1}$, ICG-PEG: 3.1, 6.3, 12.5, 25, 50, 100 $\mu\text{g mL}^{-1}$) for 24 h, followed by irradiation with an 808 nm laser (1 W cm^{-2} , 10 min) or shielding in the dark. Finally, a mixture of CCK-8 and DMEM (1 : 10) was added to each well and treated for 1 h. The absorbance was measured at 450 nm using a microplate marker.

Calcein-AM/PI staining

HeLa cells were inoculated in a glass bottomed Petri dish, and incubated with PBS, RuA₂D-P, ICG-PEG and RuPC@ICG, with or without 808 nm laser irradiation (1 W cm^{-2} , 10 min), followed by treatment with a calcein-AM/PI live-dead cell double-staining kit (Solarbio, China), with staining for 15 min, and observation using a Leica STELLARIS laser confocal scanning microscope (LCSM) at emission channels of 500–550 nm and 590–640 nm for collecting AM and PI fluorescence, respectively, under 488 nm and 535 nm excitation.

Oxygen sensitivity of RuPC@ICG at the cellular level

HeLa cells were inoculated in a glass bottomed Petri dish and sequentially incubated with RuPC@ICG (pH 7.4, 200 $\mu\text{g mL}^{-1}$) for 1 h and Dil (Beyotime, China) for 10 min, and then stained by DAPI (Beyotime, China) for 5 min. After each incubation, the Petri dishes were rinsed three times with PBS. The cells were blown by a mixed gas of O₂ and N₂ at 600 mL min^{-1} for 10 min, before the medium was replaced by PBS. Using laser confocal scanning microscopy (LCSM), the ruthenium complex (Ru) and ICG-PEG (ICG) were excited at 488 nm and 750 nm with fluorescence emission channels of 630–680 nm and 790–840 nm, respectively. DAPI and Dil were excited at 405 nm and 561 nm, with fluorescence emission channels of 425–475 nm and 540–590 nm, respectively.

In vitro cell uptake of RuPC@ICG

HeLa cells were incubated with RuPC@ICG vesicles (200 $\mu\text{g mL}^{-1}$) in PBS medium at pH 7.4 or 6.8 for 0, 10, 60, and 120 min, and then washed three times with PBS (pH = 7.4) and fixed with 4% paraformaldehyde for 15 min. Cell membranes were stained with Dil and nuclei with DAPI for observation by LCSM. The staining procedure and confocal wavelengths were chosen as described above.

Cell membrane potential

All experiments were performed on 96-well cell culture plates, and the fluorescence intensity at the emission wavelength of 525 nm was measured at an excitation wavelength of 490 nm using a microplate reader. Each well was washed with PBS solution and 100 μL of Hanks' balanced salt solution (HHBS) was added, and the membrane potential changes of HeLa cells were assessed by exposing them to the DiBAC4(3) fluorescent probe. Then, 100 μL of DiBAC4(3) solution was added at serial concentrations so that the final concentrations were 0, 50, 100, 500, 1000, and 5000 nmol L^{-1} . The fluorescence was measured every 10 min and monitored for 150 min. The objective was to find the appropriate concentration and reaction time to stabilize the fluorescence for subsequent experiments, to determine

the optimal concentration of 5 $\mu\text{mol L}^{-1}$ for the best observation time of 30 min.

To test the membrane potential changes after exposure of RuPC@ICG to HeLa cells, DiBAC4(3) was configured with DMSO as a 5 mmol L^{-1} master mix and then diluted to 5 $\mu\text{mol L}^{-1}$ with HHBS balanced salt solution. After intervention by the tested formulations for 0, 10, 20, 30, 60, 120, and 150 min, the well was washed with PBS solution and then 100 μL of 5 $\mu\text{mol L}^{-1}$ DiBAC4(3) HHBS equilibrium salt solution was added. Six replicate wells were set up for each concentration. Fluorescence was measured at wavelengths of 525 nm using a microplate reader, and interference from the background fluorescence of the ruthenium probe was subtracted.

In vivo experiments

All animal procedures were performed in accordance with the Guidelines for Care and Use of Laboratory Animals of University of Chinese Academy of Sciences and approved by the Animal Ethics Committee of University of Chinese Academy of Sciences. Male nude BALB/c mice were purchased from Beijing HFK Bioscience CO., Ltd. HeLa cells (5×10^6) suspended in 100 μL of PBS were injected subcutaneously into the right flank of mice fed in a pathogen-free environment.

After implantation for 3 days and 7 days, *in vivo* distribution studies were performed after 100 μL of RuA₂D-P (10 mg kg^{-1}) and ICG-PEG (2.5 mg kg^{-1}) or RuPC@ICG (12.5 mg kg^{-1}) were administered by intravenous injection (*i.v.*) via the tail vein, by using an *in vivo* imaging system (IVIS spectrum, PerkinElmer IVIS Lumina III, United States) equipped with fluorescence filters ($\lambda_{\text{ex}}/\lambda_{\text{em}} = 500/680$ nm and $\lambda_{\text{ex}}/\lambda_{\text{em}} = 745/820$ nm). The distribution of the fluorescent probes, *i.e.* the ruthenium complex (Ru) and ICG, was imaged at 1, 2, 4, 6, 8, 10, and 24 h after injection. Fluorescence images were pseudo-color processed using Image J and Image-Pro Plus 6.0 software. The confocal microscopy image from the Ru channel was divided by the pixel values of the ICG channel image located at the same location to obtain fluorescence intensity ratio images for the qualitative determination of the oxygen concentration distribution.

For testing the anti-tumour efficiency of the RuPC@ICG formulation, the mice were divided into four groups for receiving a dose of the RuPC@ICG liposomal formulation (two groups), RuA₂D-P and PBS by *i.v.* every two days from day 8 after tumour cell implantation for five dosages in total, among which one group of RuPC@ICG treated animals and the RuA₂D-P dosed animals also received NIR irradiation (808 nm, 1 week cm^{-2}) for 10 min in the first five dosages. All mice were assessed for body weight and tumour volume every 2 days for nine counts in total. At day 25, the animals were sacrificed, and the tumours and vital organs (heart, liver, spleen, lung and kidney) were isolated for *ex vivo* imaging and histopathological analysis.

Statistical analysis

Statistical significance was assessed using one-way ANOVA analysis on SPSS software. Differences were considered statistically



significant if the value was less than 0.05. Means and standard deviations (SD) were calculated in replicate experiments. The data were expressed as mean \pm SD.

Results and discussion

Synthesis of ruthenium complex co-assembled theragnostic liposome

The synthesis of the amphiphilic oxygen sensitive probe, *i.e.* C_n -RuA₂D-PEG, is illustrated in Fig. S1†. The ruthenium complex with two alkyl chains, *i.e.* C_n -RuA₂D, was synthesized by using alkyl chain-modified 1,10-phenanthroline-5-amine and 4,4'-diamino-2,2'-bipyridine as a ligand to coordinate a dichloro(*p*-cymene)ruthenium(II) dimer through the backflow method.⁴⁴ The obtained C_n -RuA₂D was then PEGylated *via* low-pH labile benzoic-imine linkage.¹⁸ Herein, alkyl chains with carbon numbers of 8, 12 and 18, and PEG with molecular weights of 1 kDa, 2 kDa and 5 kDa were used for the synthesis, in order to adjust the amphiphilicity for the assembly to get vesicular aggregates. In total, 5 samples were harvested, which are named C_8 -RuA₂D-PEG_{1K}, C_{12} -RuA₂D-PEG_{1K}, C_{12} -RuA₂D-PEG_{2K}, C_{12} -RuA₂D-PEG_{5K} and C_{18} -RuA₂D-PEG_{5K}, where the subscripts represent the number of carbons in the alkyl chains and the molecular weight of PEG, respectively. The chemical structures of the final products as well as the intermediate products were characterized mainly by ¹H NMR and FTIR (Fig. S2†). Meanwhile, a pH insensitive PEGylated ($M_w = 2$ kDa) C_{12} -RuA₂D was also prepared for comparison *via* amidation (Fig. S3†). Additionally, PEGylated ICG was synthesized by reacting ICG-NHS with mPEG-NH₂ ($M_w = 2000$ Da). The aim of PEGylation is to improve the solubility of ICG in an aqueous solution and increase the molecular weight, or the size of the photosensitizer for slower release from the delivery vehicle, *i.e.* liposomes, after encapsulation. The structure of the ICG-PEG was confirmed by ¹H NMR and FTIR (Fig. S2†).

The self-assembly and co-assembly behaviours of C_n -RuA₂D-PEG with PC were then investigated (Scheme 1). TEM images show that C_{12} -RuA₂D-PEG_{1K} and C_{12} -RuA₂D-PEG_{2K} generated vesicular aggregates in aqueous solution through a solvent evaporation method with hydrodynamic diameters of 127 nm and 134 nm (DLS), whereas the other samples formed particulate aggregates (Fig. 1A and S4†), mainly attributed to the hydrophilic-lipophile balance of the amphiphiles. Due to the vesicle-forming tendency, C_{12} -RuA₂D-PEG_{2K} was used for the co-assembly with PC to generate oxygen sensitive probe-labelled liposomes, namely RuPC, with pH responsiveness owing to the low pH-labile characteristics of the benzoic-imine linkage between RuA₂D and PEG. In addition, cholesterol (CHOL) was involved in the co-assembly to favour the liposome formation by increasing the hydrophobic interactions among the alkyl chains.⁴⁵ With C_{12} -RuA₂D-PEG_{2K}:PC:CHOL mass ratios of 1:1:0.1, 2:1:0.1 and 5:1:0.1, co-assembled liposomes were observed by TEM, as shown in Fig. 1B, with particle sizes of 186 nm, 254 nm and 296 nm (Fig. S4†). The ICG-PEG encapsulated RuPC liposomes

(RuPC@ICG) with a C_{12} -RuA₂D-PEG_{2K}:PC:CHOL ratio of 2:1:0.1 were then prepared (Fig. 1C). The vesicular architecture of the RuPC@ICG liposome as well as the cavity location of ICG-PEG were observed by LCSM, where a circular shape in the fluorescence image can be seen from the ruthenium complex emission together with the enclosed ICG fluorescence pattern (Fig. 1D), and this was additionally proven by TEM (Fig. 1D). The loading capacity of ICG-PEG was determined to be 11.4 wt%. The RuPC@ICG liposome displays a size of 396 nm at pH 7.4 (Fig. 1E), larger than that of the corresponding empty RuPC liposome at the same pH, *i.e.* 254 nm (Fig. 1F).

It is well known that the preparation procedure can influence the formation of liposomes or vesicles from amphiphiles. In this work, directly dispersing C_{12} -RuA₂D-PEG_{2K} in PBS (pH = 7.4) by sonication could allow the harvest of particulate nano-aggregates (RuA₂D-P) with a size of about 91 nm (Fig. 1B and E), which is different from the self-assembled C_{12} -RuA₂D-PEG_{2K} vesicles (RuA₂D-V) generated through the solvent evaporation method (Fig. 1A and S4†). The particulate nano-aggregate was used as a control sample for the following study. In addition, as ICG-PEG is also amphiphilic, micellar aggregates of ICG-PEG were also formed with a size of 59 nm (Fig. 1E).

The pH sensitivities of RuPC liposomes and their formulations, *i.e.* RuPC@ICG, were tested by treating at pH 7.4 and 6.8, simulating the physiological pH and the extracellular pH of the solid tumour.¹⁵ Fig. 1F and S5† show that the particle size of RuPC as well as RuA₂D@ICG only slightly decreased upon the pH change from neutral to mildly acidic. Meanwhile, the vesicular structure of both samples was preserved under acidic conditions, according to TEM (Fig. S5†). In contrast, the zeta potential of the liposomes, *e.g.* RuPC, significantly increases from very negative at pH 7.4, *i.e.* -14.1 mV, to mildly positive at pH 6.8, *i.e.* +2.1 mV (Fig. 1F). Liposomes formed by PC normally show negative charge nature in aqueous solution at neutral pH.³⁷ The zeta potential remained at a negative value even after the co-assembly with the ruthenium complex amphiphile, *i.e.* C_{12} -RuA₂D-PEG_{2K}, at a mass ratio of 2:1 to PC, indicating that the PEG chains are unable to shield the charged groups of PC molecules. A negatively charged surface is beneficial for the liposome to avoid recognition by immunological systems. At pH 6.8, the PEG chain detached from the liposome surface due to the cleavage of the benzoic-imine bond and hence exposed positively charged amine groups (Fig. 1C and F). To further prove the pH sensitivity of the RuPC liposome, pH insensitive PEG-conjugated C_{12} -RuA₂D was synthesized by PEGylation through amidation. As expected, its co-assembled liposome showed no significant difference in size or zeta potential between pH 7.4 and 6.8 (Fig. S6†). The results suggest that the pH sensitive RuPC liposomes may be able to reduce the repulsion force of the cell membrane in a hypoxic tumour tissue.

Fluorescence spectra related to RuPC@ICG are shown in Fig. 1G-J. The excitation of C_{12} -RuA₂D-PEG_{2K} results in a peak at 470 nm, under which an emission peak is present at around 660 nm, which overlaps the excitation peak of ICG-PEG,



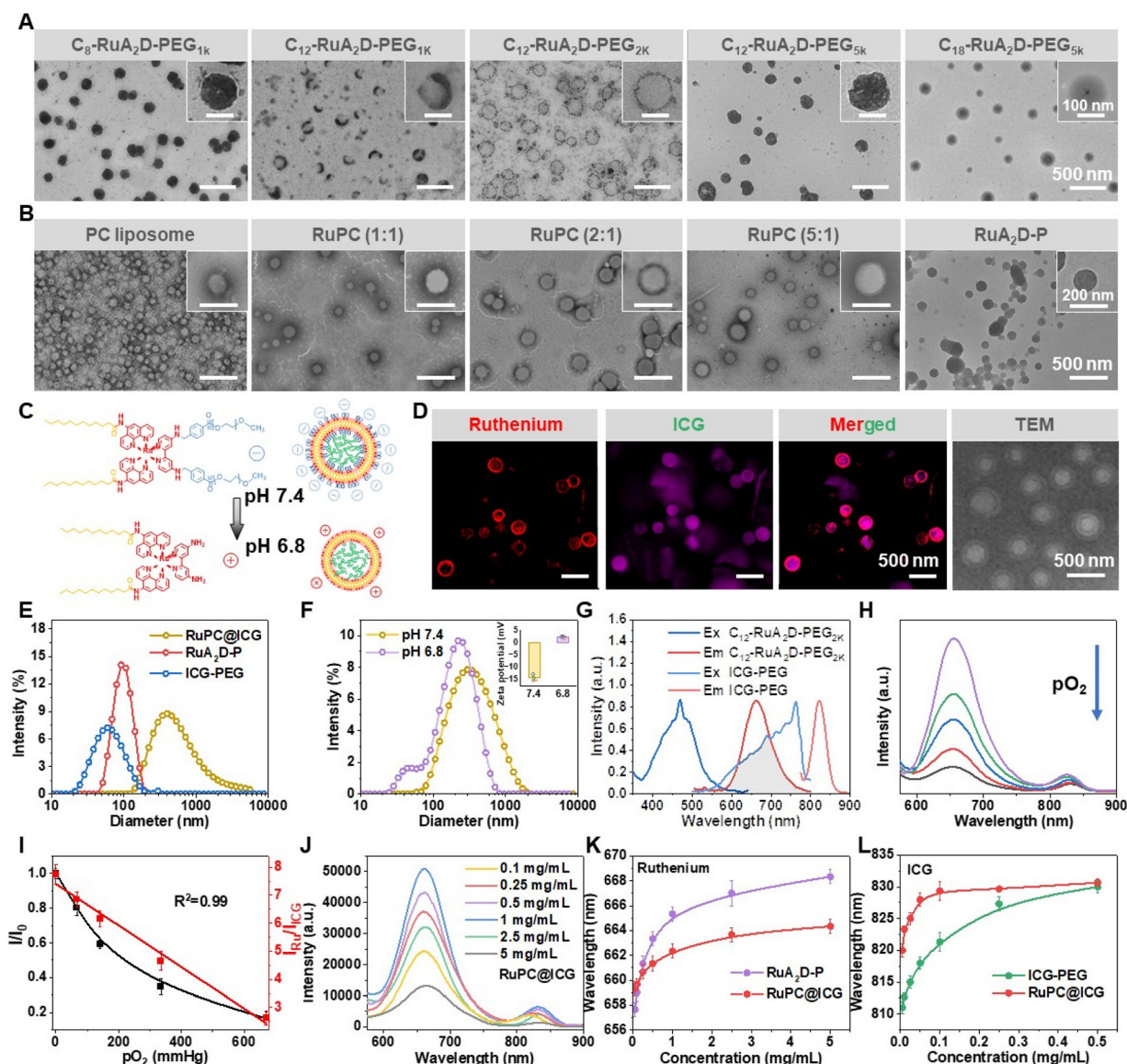


Fig. 1 (A) TEM images of self-assemblies formed by the amphiphilic ruthenium complex with different chain lengths of the hydrophilic and hydrophobic groups. (B) TEM images of phosphatidylcholine (PC) liposomes, co-assemblies formed by C_{12} -RuA₂D-PEG_{2K} and PC at different mass ratios (RuPC), with a constant amount of cholesterol (CHOL), *i.e.* 0.1 (w/w) to PC, and particulate aggregates of C_{12} -RuA₂D-PEG_{2K} prepared by sonication (RuA₂D-P). (C) Illustrated structures of C_n -RuA₂D-PEG and ICG-PEG encapsulated RuPC (RuPC@ICG) liposomes and their pH sensitivity originating from the low-pH labile nature of the benzoic-imine linkage. (D) LCSM and TEM images of RuPC@ICG at pH 7.4. The feed ratio of C_{12} -RuA₂D-PEG_{2K} : PC : CHOL was 2 : 1 : 0.1, and the loading capacity of ICG-PEG was 11.4 wt%. (E) DLS of RuPC@ICG, ICG-PEG and RuA₂D-P in PBS at pH 7.4. (F) DLS and zeta potential of co-assembled C_{12} -RuA₂D-PEG_{2K} (RuPC) liposomes in PBS at pH 7.4 and 6.8. (G) Excitation and emission spectra of C_{12} -RuA₂D-PEG_{2K} and ICG-PEG. (H) Fluorescence emission spectra of RuPC@ICG (200 μ g mL⁻¹) with 0, 67, 140.7, 335 and 670 mmHg of pO₂ (λ_{ex} = 470 nm). (I) Relative fluorescence intensity of the ruthenium complex in RuPC@ICG and the intensity ratio of the ruthenium complex to ICG as a function of pO₂. (J) Fluorescence emission spectra of RuPC@ICG at different concentrations (λ_{ex} = 470 nm). (K and L) Concentration dependent peak position of ruthenium (K) and ICG (L) from emission spectra of RuPC@ICG compared with that of RuA₂D-P and ICG-PEG dispersions.

suggesting a possible FRET effect between the two fluorophores (Fig. 1G). ICG-PEG shows emission with a maximum intensity at 820 nm. Due to the inclusion of the ruthenium complex, the fluorescence intensity of the RuPC@ICG liposome is dependent on the oxygen concentration in the aqueous medium. Fig. 1I shows that the relative fluorescence intensity of ruthenium at 660 nm (I/I_0) decreases with the

increase of the oxygen partial pressure in solution. Nonetheless, for monitoring the oxygen level *in vivo*, ratio-metric measurement is preferred because of the independence of probe concentration.^{25,27} As seen in Fig. 1I, the intensity ratio of the ruthenium complex to ICG, *i.e.* I_{Ru}/I_{ICG} , also correlates to the oxygen concentration, and gives a linear relationship that simplifies the measurement.



The influence of concentration on the emission spectra of the RuPC@ICG liposome is shown in Fig. 1J. Apart from the phenomenon of aggregation caused quenching (ACQ), it is noted that there is a bathochromic shift of the emission wavelength from both the ruthenium complex and ICG with the increase of the probe concentration, which probably originates from the close packing of the fluorophores. Therefore, the wavelengths for the maximum intensity for the ruthenium complex and ICG emission from the co-assembled RuPC@ICG liposome (Fig. S7†) were compared with the directly dispersed RuA₂D-P or ICG-PEG in aqueous solution as a function of probe concentration, showing that at the same probe concentration, the ruthenium peak of RuPC@ICG has a lower wavelength than that of the RuPC aggregate, whilst the ICG peak shows a higher wavelength than that of ICG-PEG (Fig. 1K and L). These results prove that C₁₂-RuA₂D-PEG_{2K} was well-distributed in the lipid layer, which was separated by PC molecules in RuPC@ICG, preventing the close packing of ruthenium complex moieties. Meanwhile, it also indicates the encapsulation of ICG-PEG in RuPC@ICG, leading to a higher probe concentration inside the cavity, and therefore a red shift of the fluorescence spectrum compared to that of the homogeneously dispersed ICG-PEG at the same apparent concentration.

Membrane fusion performance of RuPC@ICG liposome

The internalization of RuPC@ICG liposomes to cancer cells was elucidated on the HeLa cell line, by incubation at 37 °C and pH 7.4 for 10–120 min. Using LCSM, a gradual enhancement of ruthenium fluorescence in the cell membrane area is revealed, highly overlapped with the Dil fluorescence (Fig. 2A). Additionally, the distribution of the ICG fluorescence is very different from that of the ruthenium when incubated using RuPC@ICG with the HeLa (Fig. 2A). While the ruthenium fluorescence keeps accumulating near the cell membrane, ICG fluorescence demonstrates an outside-in process, that is, initially distributing in the membrane area, colocalized with ruthenium, and subsequently internalizing and eventually distributing in the cytoplasm within 120 min (Fig. 2A and B). Dil and DAPI were used to stain the cell membrane and nucleus, respectively. In addition, it is shown that under mildly acidic conditions, *i.e.* pH 6.8, the cell uptake of ICG could be accelerated from the RuPC@ICG liposomes (Fig. 2C). Quantitative integration of ruthenium and ICG fluorescence shows an increase in fluorescence intensity over time, with a faster rate of entry into the cell in a weakly acidic environment, where the ruthenium fluorescence intensity at pH 6.8 (10 min) is 1.3 times higher than at pH 7.4, and the ICG fluorescence intensity at pH 6.8 is 3.14 times higher than at pH 7.4 (Fig. 2D and E), which is reasonable since the cell-liposome interaction becomes stronger once the liposome surface is less negatively charged.

The membrane distribution of the probing amphiphile, *i.e.* C₁₂-RuA₂D-PEG_{2K}, suggests a membrane fusion pathway of RuPC@ICG liposomes for the transportation of ICG-PEG into cells (Fig. 2F).^{46–48} To further prove this, a membrane potential

fluorescent probe DiBAC4(3) was incubated with RuPC@ICG liposomes with different contents of C₁₂-RuA₂D-PEG_{2K} for monitoring the fluorescence at 525 nm ($\lambda_{\text{ex}} = 490 \text{ nm}$). DiBAC4(3) incorporated self-assembled RuA₂D@ICG vesicles and particulate RuA₂D-P aggregates were used as control samples. The fluorescence intensity of DiBAC4(3) increases in the case where the cell membrane potential decreases, causing inward flow of the fluorescent dye.^{49,50} According to Fig. 2G, the OD values of DiBAC4(3) display an obvious increase and then a subsequent decrease within 60 min for all the vesicular formulations, whereas the particulate formulation resulted in only a slight increase of OD within the time period. Moreover, liposomes with a higher content of RuPC including the neat C₁₂-RuA₂D-PEG_{2K} vesicles (RuA₂D-V) exhibit higher amplitudes of OD increase. This phenomenon can be explained by the membrane fusion of the vesicles, by which the C₁₂-RuA₂D-PEG_{2K} molecules were bound by the cell membrane without disrupting its integrity,⁵¹ and therefore the PEG chains could temporarily shield the charged groups of the phospholipids. Additional experiments on the incubation of ICG-PEG encapsulated RuA₂D-V vesicles with HeLa cells showed similar ICG internalization *via* a membrane fusion pathway, *i.e.* membrane distribution of ruthenium fluorescence and the cytosol distribution of ICG fluorescence (Fig. S8†). In contrast, the particulate C₁₂-RuA₂D-PEG_{2K} (RuA₂D-P) taken up *via* an endocytosis pathway, evidenced by the cytosol distribution of ruthenium fluorescence (Fig. S9†), caused less disruption to the membrane potential of the cells (Fig. 2G).

Photothermal effect and cellular oxygen imaging ability of RuPC@ICG

To verify the photothermal properties of ICG in RuPC@ICG liposomes, infrared thermography was utilized to record the temperature changes of the PBS dispersion, with RuA₂D-P aggregates, and ICG-PEG dispersions as control samples, which were irradiated by an 808 nm laser at 1 W cm⁻² for 0, 2, 4, 6, 8 and 10 min. As expected, RuPC@ICG warmed up the fastest, reaching 54.9 ± 0.4 °C from an initial temperature of 25.2 ± 0.1 °C after just 10 min, whereas the temperature of neat PBS only slightly changed by 1.5 ± 0.3 °C (Fig. 3A and B). Meanwhile, the temperature of RuA₂D-P and ICG-PEG dispersions increased to 29.7 ± 0.4 °C and 51.1 ± 0.2 °C, respectively (Fig. 3A and B). The photothermal warming curves of RuPC@ICG liposomes at different concentrations and different powers were also determined (Fig. S10†). The results indicate that the photothermal effect mainly originated from the ICG moiety. The RuPC@ICG liposomes also exhibited good photothermal stability. After five heating and cooling cycles, the equilibrium temperature under irradiation was around 52.3 °C, with only a negligible decrease compared to that after the first heating (Fig. 3C). Inspired by the generation of ¹O₂, the photodynamic therapy (PDT) performance of RuPC@ICG liposomes was measured by electron spin resonance (ESR) using 2,2,6,6-tetramethylpiperidine (TEMP) as a trapping agent. As shown in Fig. 3D, the appearance of a ¹O₂ peak was observed in the ESR spectrum after the sample was



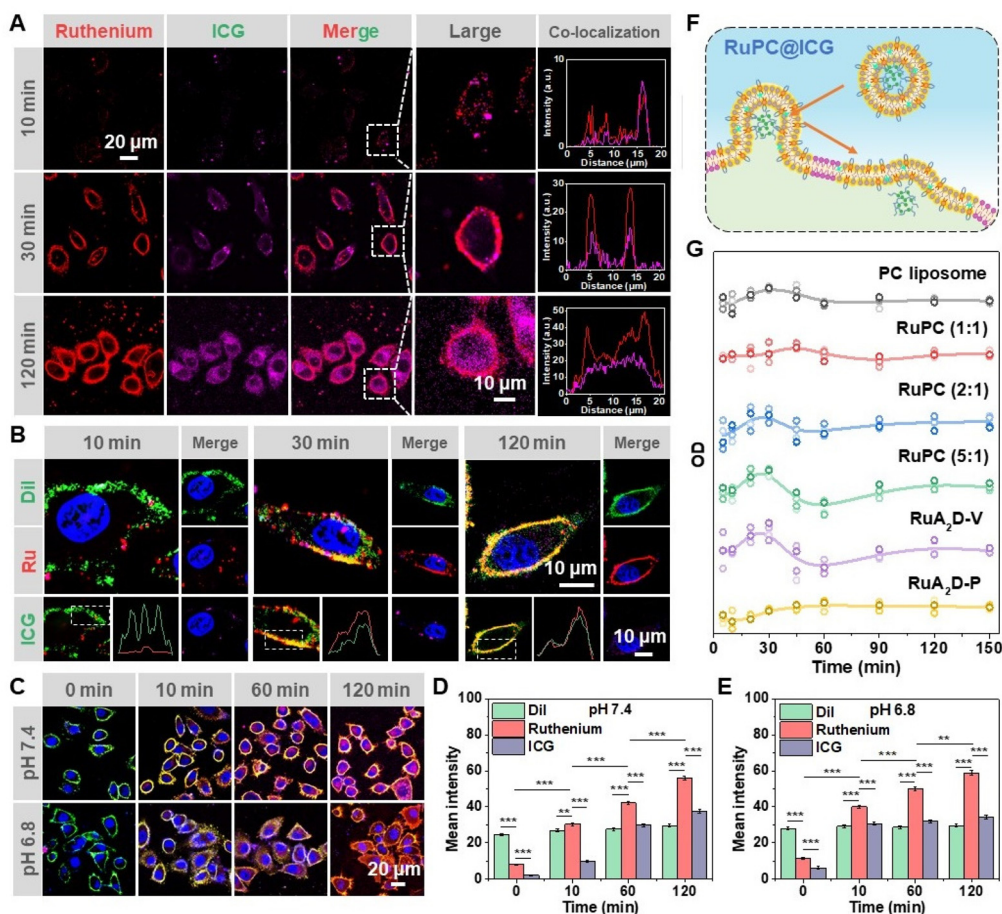


Fig. 2 (A) LCSM of HeLa cells after incubation with RuPC@ICG liposomes for different time periods at pH 7.4. (B) Colocalization of DAPI fluorescence (405 nm, blue), ruthenium (Ru) fluorescence (488 nm, red), Dil fluorescence (538 nm, green) and ICG fluorescence (750 nm, magenta) on HeLa cells after incubation with RuPC@ICG for different time periods. (C) LCSM of HeLa cells cultured with RuPC@ICG at pH 7.4 and 6.8. (D and E) Integral of the fluorescence intensity from Dil, ruthenium and ICG channels recorded from (C) at pH 7.4 (D) and pH 6.8 (E). (F) Schematic diagram of the internalization pathway of RuPC@ICG. (G) OD values of DiBAC4(3) as a function of incubation time of RuPC@ICG with HeLa cells.

irradiated by an 808 nm laser for 10 min. The ability to generate $^1\text{O}_2$ is in the order RuPC@ICG liposome > ICG-PEG dispersion > RuA₂D-P (Fig. 3D). Overall, the photosensitivity effect was examined on the HeLa cell line with calcein AM/propidium iodide (PI) double staining. It can be seen in Fig. 3E, under NIR (808 nm) irradiation, that serious apoptosis can be recognized after incubation with ICG-PEG or RuPC@ICG, with the emission of red fluorescence from a major portion of the cells. In comparison, RuA₂D-P has only minor phototoxicity (Fig. 3E). Furthermore, the cell viability with RuPC@ICG liposomes, ICG-PEG dispersion and RuA₂D-P was assessed using CCK-8 assay on the same cell line. While cell viability of over 90% was achieved for all the samples without NIR irradiation, the cell viability decreases to 77.2%, 16.4% and 10.2% at the highest concentration, *i.e.* 1000 $\mu\text{g mL}^{-1}$, for RuA₂D-P, ICG-PEG and RuPC@ICG liposomes, respectively, upon NIR irradiation for 10 min (Fig. 3F and G). Considering that the cell viability for ICG-PEG and RuPC@ICG liposomes have significant differences ($p < 0.05$) (Fig. 3G), we suggest that RuPC@ICG liposomes can cause synergistic effects for PTT and PDT.

The capacity of the RuPC@ICG liposomes for ratiometric imaging of the hypoxic condition at the cellular level was then evaluated on the HeLa cell line (Fig. 3H). RuPC@ICG was incubated with the cells in the culture medium at different oxygen partial pressure (0, 67, 140.7, 335 and 670 mmHg) at 37 °C and pH 7.4 for 1 h. Once again, the ruthenium complex was found distributed mainly in the cell membrane while ICG was delivered into the cell, as demonstrated by LCSM (Fig. 3H and S11†). The oxygen concentration change can be recognized by observing the change in the ruthenium fluorescence, significantly decreasing with the increase in oxygen concentration, whilst there is little change for the ICG fluorescence (Fig. 3H). This was confirmed after quantitatively integrating the fluorescence intensity from the ruthenium channel and the ICG channel (Fig. 3I). This shows that the intensity ratio of ruthenium to ICG ($I_{\text{Ru}}/I_{\text{ICG}}$) still has a linear relationship with the variation of oxygen partial pressure in the medium ($R^2 = 0.98$) (Fig. 3J). Despite the distribution of the ruthenium complex and ICG not being colocalized in the cell region, the ratiometric measurement of the hypoxia condition can be valid



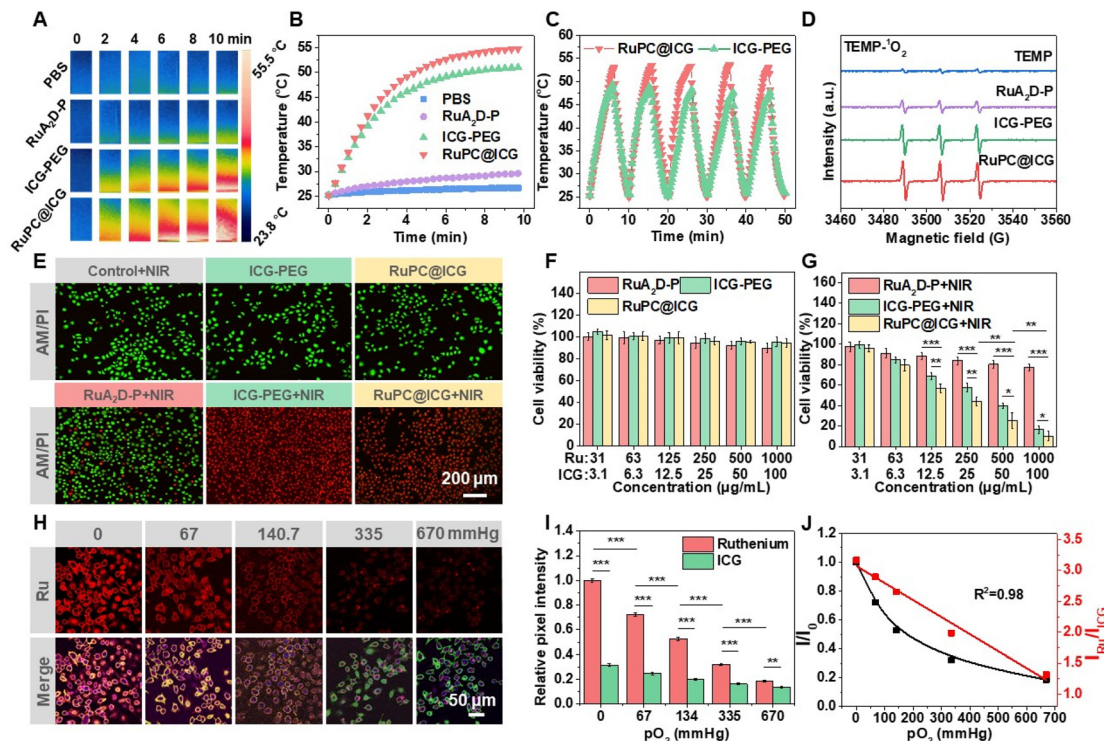


Fig. 3 (A) Photothermal efficiency of PBS (pH = 7.4, 0.01 M), RuA₂D-P (200 $\mu\text{g mL}^{-1}$), ICG-PEG (200 $\mu\text{g mL}^{-1}$) and RuPC@ICG (200 $\mu\text{g mL}^{-1}$) irradiated by an 808 nm laser (1 W cm^{-2}) captured by a thermal camera. (B) The photothermal conversion curves of the tested materials, *i.e.* temperature versus irradiation time, captured by a paperless recorder. (C) Photothermal stability of RuPC@ICG compared with ICG-PEG. (D) ESR spectra of PBS, RuA₂D-P, ICG-PEG, and RuPC@ICG (200 $\mu\text{g mL}^{-1}$) mixed with TEMP. (E) LSCM images of calcein (AM, green) and propidium iodide (PI, red) stained HeLa cells after incubation with different samples, with or without irradiation by an 808 nm laser. (F and G) CCK-8 assay of HeLa cells after incubation with RuA₂D-P, ICG-PEG or RuPC@ICG at different concentrations in the absence of light (F) or with irradiation at 808 nm (1 W cm^{-2}) for 10 min (G) followed by incubation for 24 h. (H) LSCM of HeLa cells after 1 h of coexistence with RuPC@ICG vesicles (pH 7.4, 200 $\mu\text{g mL}^{-1}$) in a medium solubilized with 0, 67, 140.7, 335 and 670 mmHg pO₂. Ru represents the ruthenium channel which was excited at 488 nm and emission was recorded from 630 nm to 680 nm, while Merge represents the merged fluorescence of ruthenium and ICG ($\lambda_{\text{ex}} = 750 \text{ nm}$, $\lambda_{\text{em}} = 790\text{--}840 \text{ nm}$). (I) Integral of the fluorescence intensity from the ruthenium and ICG channels. The strongest pixel signal intensity of the HeLa cell images under 0 mmHg pO₂ was defined as 1.0. (J) Calibration curve of the oxygen response of RuPC@ICG at the cellular level. Statistical analysis: * $p < 0.05$, ** $p < 0.01$, *** $p < 0.001$.

when the RuPC@ICG liposomes were delivered to the targeted cells.

In vivo solid tumour detection using RuPC@ICG

HeLa tumour-bearing male BALB/c mice were used for validating the diagnosis capacity of RuPC@ICG liposomes *in vivo*. After cancer cells were implanted in the right flanks of the animals for 3 or 7 days, the formulation was administrated *via* intravenous injection to the tail vein and the photoluminescence from the living animals was imaged at scheduled time points from 1 h to 24 h after injection. Other than the RuPC@ICG liposomes, a mixture of particulate RuA₂D-P and ICG-PEG, working as a combined diagnostic agent, was used as a positive control. The pseudo colour images based on the fluorescence imaging from ruthenium and ICG channels, and their ratiometric images are plotted in Fig. 4A–F, corresponding to the formulations of liposomes and the combined-probe mixture, as well as the observation time points at day 3 and day 7.

By comparing Fig. 4A and B, it can be seen that after tumour implantation for 3 days, the liposome formulation resulted in the accumulation of fluorescence emission at the implantation site of the animals, *i.e.* the right flank, and the ICG channel has better signal to noise ratio (Fig. 4B). In contrast, the signal at the tumour site is hardly distinguishable from that for the group treated with the combined-probe formulation at this time point (Fig. 4A). Nevertheless, it should be pointed out that except for a visible contour, the fluorescence intensity is not the strongest in the tumour area from RuPC@ICG (Fig. 4B). Higher emission intensity was observed in the abdomen region, from both ruthenium and ICG channels, showing at least three high signal regions around the stomach, liver and kidney areas, which is quite reasonable from the view of metabolism.⁵² In early-stage tumour diagnosis, the identification of the tumour site among healthy tissues is considered to be essential. Although the pH sensitivity might be helpful for the RuPC@ICG liposomes to more efficiently accumulate at the tumour site, since the construction of blood vessels would be incomplete in a tiny tumour, it



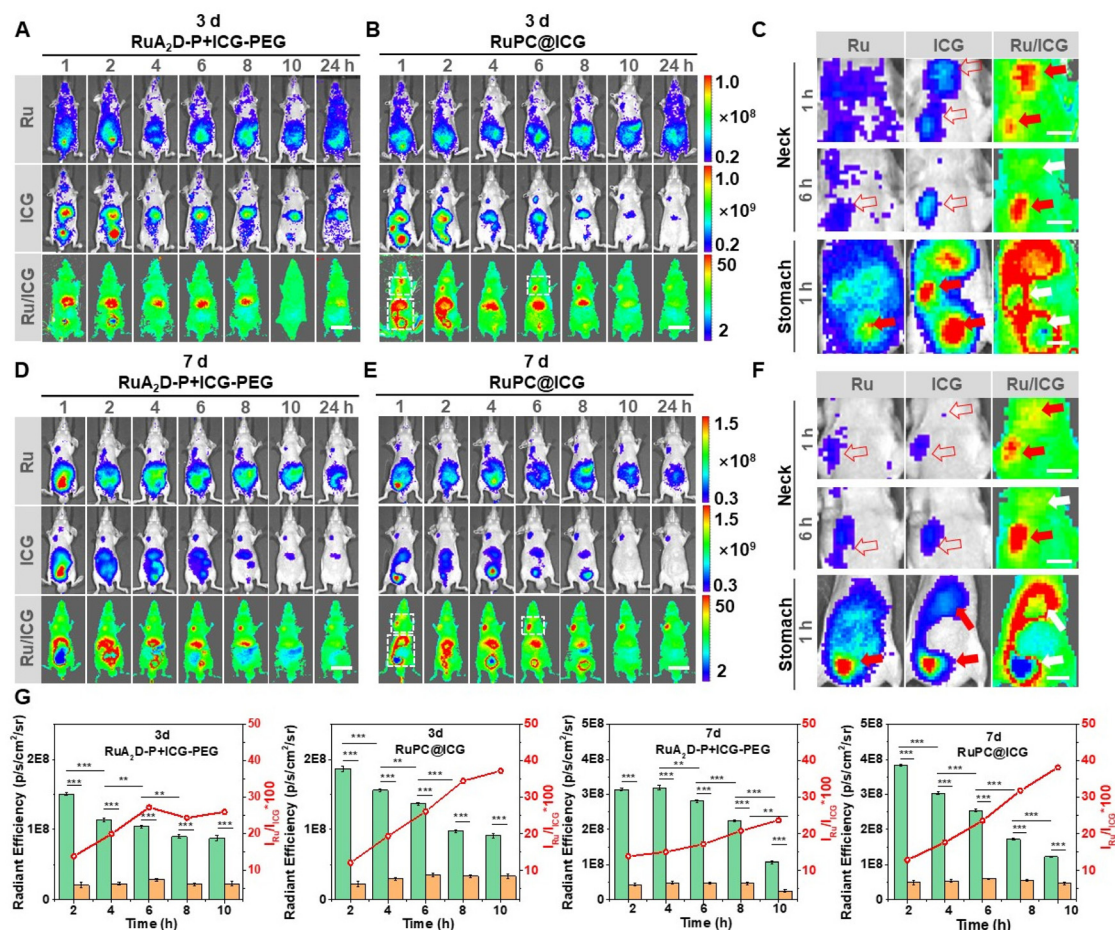


Fig. 4 (A and B) *In vivo* fluorescence images for observing ruthenium (Ru) and ICG fluorescence from tumour-bearing mice after *i.v.* injection of a mixture of RuA₂D-P and ICG-PEG (A) or RuPC@ICG formulation (B) 3 days after the implantation of cervical cancer (HeLa) cells. Ru/ICG shows the ratiometric image (scale bar = 2 cm). (C) Magnified *in vivo* fluorescence images from the positions surrounded by white rectangles in (B) (scale bar = 5 mm). (D and E) *In vivo* fluorescence images for observing ruthenium (Ru) and ICG fluorescence from tumour-bearing mice after *i.v.* injection of a mixture of RuA₂D-P and ICG-PEG (D) or RuPC@ICG formulation (E) 7 days after the implantation of cervical cancer (HeLa) cells (scale bar = 2 cm). (F) Magnified *in vivo* fluorescence images from the positions surrounded by white rectangles in (E) (scale bar = 5 mm). (G) Integral of the fluorescence intensity or the intensity ratio (I_{Ru}/I_{ICG}) from tumour regions in the fluorescence images. Yellow bars: Ru fluorescence, green bars: ICG fluorescence. Red lines: I_{Ru}/I_{ICG} . Statistical analysis: ** $p < 0.01$, *** $p < 0.001$.

should be the capacity of co-delivery of the two probes, *i.e.* the ruthenium complex and ICG, rather than a site-specific delivery, that allows the determination of the tumour suspect region from the false-positive regions, by achieving ratiometric imaging.

The ratiometric signal and the metabolic process of the probes were monitored. By measuring I_{Ru}/I_{ICG} , the ratiometric images from the RuPC@ICG group reveal that the high signal regions in the abdomen actually have higher oxygen concentrations, *i.e.* normoxia condition with lower I_{Ru}/I_{ICG} values (Fig. 4B and C), which is inconsistent with the characteristics of anaerobic glycolysis occurring in tumour tissue. In contrast, the ratiometric measurement in the liposome treated group focuses on two hypoxia regions in the flank and neck areas at 1 h after administration (Fig. 4C). However, as time passed, the signal in the neck area decayed rapidly and disappeared within 4 h (Fig. 4B). The fast fading is attributed to the distrib-

uted liposomes in the lymph.⁵³ In comparison, the ratiometric signal in the tumour site is quite stable, and is visible even after 24 h (Fig. 4B), implying long preservation of the probe and a low oxygen concentration in the tumour tissue. At day 7 after tumour cell implantation, the signal-to-noise ratio of the ruthenium complex as well as ICG at the tumour site becomes much higher, although the abdomen biodistribution of the probes is also serious (Fig. 4D and E). The tumour signal could be revealed even using the combined-probe formulation (Fig. 4D). For the liposome formulation, the signal at the tumour site becomes the strongest one after injection for 10 h (Fig. 4E and F). The average size of a tumour has been measured to be $20.1 \pm 2.4 \text{ mm}^3$ on the 3rd day, and increased to $29.6 \pm 4.1 \text{ mm}^3$ on day 7, an increase of 47%.

For the metabolic process of the probes, whether from the RuPC@ICG liposomes or the combined-probe formulation, quantitative integration determines the decrease of ICG inten-



sity with time, while the I_{Ru}/I_{ICG} value remains at a high level for at least 10 h (Fig. 4G), inferring that the dual-probe liposome could efficiently monitor the tumour hypoxia for a prolonged time interval even though the local concentration of the probe decreased following the metabolism. It is noted that the absolute intensity of the ruthenium and ICG fluorescence is higher on day 7 than on day 3 at each metabolic time point from 1 h to 24 h, whereas the I_{Ru}/I_{ICG} values are similar (Fig. 4G), an indication of favourable uptake of the liposomes or the probes by a larger tumour grown for a longer time. Nevertheless, the RuPC@ICG liposomes enable the detection of a solid tumour at an early stage through the ratiometric method, which is more sensitive than the measurement of fluorescence intensity. Compared to the combined-probe formulation, the liposome formulation allowed better enrichment of the probes in the tumour tissue, probably due to the ability to fuse into the cell membrane and hence achieve higher efficiency to deliver the probes to cells. Since a broad distribution of diagnostic agents is acceptable in practice for the discovery of a tumour position, our results indicate that dynamic observation of the evolution of the fluorescence signal, especially related to the oxygen concentration, would improve the accuracy of tumour diagnosis. Herein, a high

hypoxia signal with a slow decay process indicates a high risk of tumour generation.

In vivo tumour growth inhibition ability of RuPC@ICG

After the tumour site was identified, the therapeutic efficiency of RuPC@ICG was evaluated on the tumour bearing BALB/c mice from day 8 after the cancer cell implantation when the tumour volume was $34.1 \pm 1.3 \text{ mm}^3$. With the main purpose being testing optically positioned PTT, the animals were divided into four groups, two of which received a dose of the RuPC@ICG liposomes, with or without NIR irradiation, and two control groups, which were dosed with particulate RuA₂D-P aggregates or PBS, without the inclusion of ICG, but received NIR irradiation. The treatment was carried out every two days five times including phototherapy (808 nm, 1 W cm^{-2} , 10 min), and measurement of the tumor size and weight was carried out every two days for a total of nine times (Fig. 5A).

Fluorescence imaging has proven that the ICG moiety could be delivered by RuPC@ICG liposomes with enhanced accumulation at the tumour site during the tumour growth period from day 3 to day 7 (Fig. 4). Herein, *ex vivo* fluorescence images of the resected tumours and major organs confirm predominant luminescence distribution at the tumour sites of the

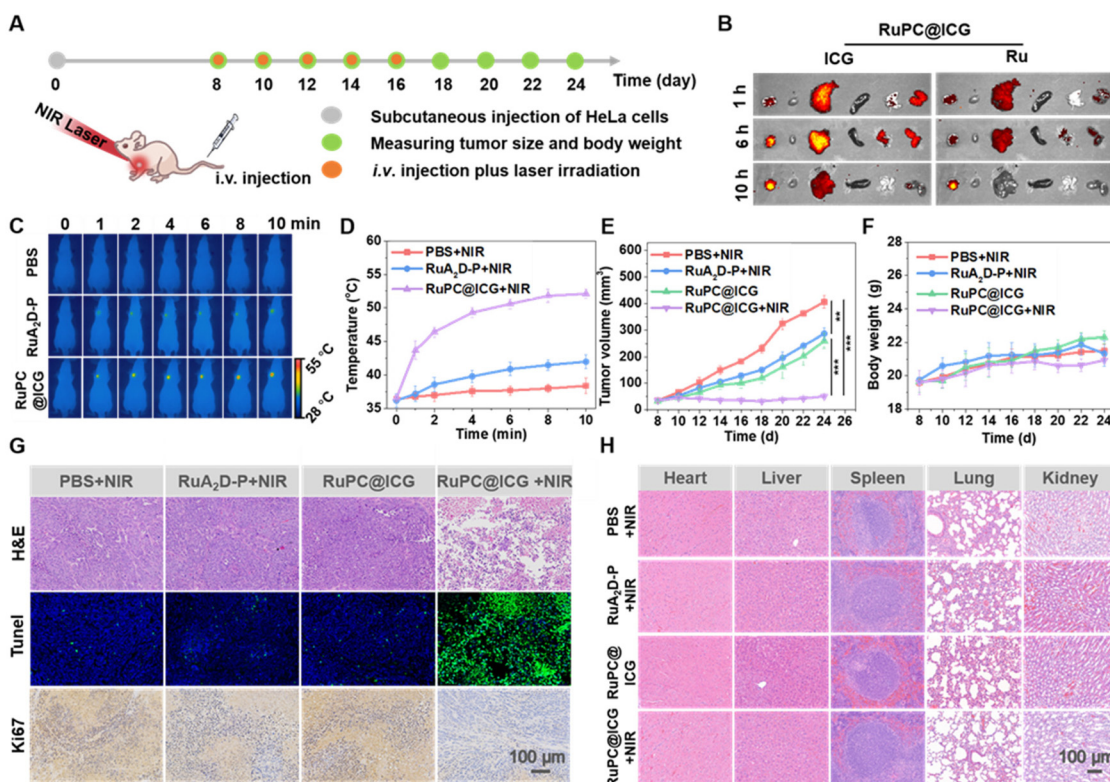


Fig. 5 (A) Illustration of the timeline for the *in vivo* anti-tumour experiment ($n = 3$). (B) *Ex vivo* fluorescence images of tumours and major organs after intravenous injection of RuPC@ICG (12.5 mg kg^{-1}). (C) Infrared images of animals dosed with PBS (pH = 7.4, 0.01 M, 0.1 mL), RuA₂D-P (10 mg kg^{-1} , 0.1 mL) and RuPC@ICG (12.5 mg kg^{-1} , 0.1 mL) after irradiation by an 808 nm laser (1 W cm^{-2}) for different times. (D) Dynamics of temperature increase as a function of irradiation time analysed from (C). (E) Tumour growth curves of mice treated with different formulations with or without thermal therapy. (F) Evolution of body weights of tumour-bearing mice during the treatment. (G) H&E, TUNEL and Ki67 stained sections of tumour tissues after 24 days of different treatments. (H) H&E sections of major organs of mice. Statistical analysis: $**p < 0.01$, $***p < 0.001$.



animals, after dosing by RuPC@ICG, and the fluorescence intensity increased over time from 1 h to 10 h after administration (Fig. 5B and S12†). The probe accumulation is mainly in the liver, which is an organ for digesting nanoparticles,⁵⁴ showing the highest fluorescence at 6 h, with faster clearance than in tumour tissue (Fig. 5B and S12†). The process is similar to that observed for living animal imaging (Fig. 4B and E). As a result, the photothermal effect of the RuPC@ICG liposomes upon NIR irradiation is demonstrated in Fig. 5C and D. Within 10 min of NIR irradiation, the temperature of the irradiated area in the animals dosed with RuPC@ICG increased to 52.1 ± 0.7 °C from 36.4 ± 0.6 °C, whilst it was 42.0 ± 0.8 °C and 38.4 ± 1.2 °C for the mice dosed with RuA₂D-P and PBS.

The tumour growth inhibition efficiencies by different treatments are shown in Fig. 5E. After 24 days of observation, it is found that phototherapy with RuPC@ICG achieved the best prognosis, and had minimized the tumour growth to 43.2 ± 7.2 mm³, only slightly larger than the initial size, *i.e.* 34.2 ± 1.3 mm³. In contrast, in the PBS + NIR group, the tumour grew to 406.3 ± 23.5 mm³. In comparison, the treatment with RuPC@ICG liposomes in the absence of NIR and the group treated by particulate RuA₂D-P aggregates with NIR irradiation led to limited inhibition of tumour growth (Fig. 5E). The tumour sizes increased to 286.3 ± 21.1 mm³ and 259.8 ± 27.8 mm³ on the 24th day, respectively, without statistical difference between each other ($p > 0.05$), but significantly smaller than the control (PBS + NIR) group ($p < 0.01$) and significantly larger than the sample (RuPC@ICG + NIR) group ($p < 0.001$). It is noted that during the treatment, all animals were well tolerated without obvious increase or decrease in body weight (Fig. 5F). Histopathological and immunological staining by H&E, TUNEL and Ki67 on the tumour sections clearly show the apoptosis of cancer cells in the tumour tissue after treatment by RuPC@ICG liposomes in the presence of NIR irradiation, whereas treatment with RuPC@ICG liposomes and RuA₂D-P + NIR only caused limited cell death in the tumour tissue (Fig. 5G). Although the literature describes the anti-cancer effect of ruthenium complexes as a metallodrug effect,^{55,56} the effect is not pronounced in this work. The inhibition of tumour growth should mainly originate from the PTT effect, possibly synergized with the PDT effect of ICG. Finally, the safety of RuPC@ICG was examined through H&E, which proved that no serious cytoarchitectural alterations, pathological changes, or organ damage was observed in the major organs like kidney, lung, spleen, liver and heart (Fig. 5H).

Conclusions

In conclusion, we synthesized an amphiphilic ruthenium complex containing two alkyl chains and being PEGylated *via* a benzoic-imine linkage, which was used as an oxygen sensitive fluorescent probe to co-assemble with phosphatidylcholine for the preparation of theragnostic liposomes with the encapsulation of PTT agent ICG-PEG. The harvested RuPC@ICG is tumour pH_e responsive and is able to interact

with cancer cells through membrane fusion, simultaneously binding the ruthenium complex amphiphile in the cell membrane and delivering ICG-PEG into the cytoplasm. Through such a pathway, the RuPC@ICG liposomes favourably accumulated at the tumour site of the mouse model. Early-stage tumour diagnosis could be thus performed using a ratiometric imaging technique to distinguish the tumour location from normal tissues. Furthermore, the detected solid tumour could be treated with NIR irradiation for photothermal therapy, which efficiently limited the tumour growth while resulting in no side effects on other organs. Our work provides a facile method for the future development of theragnostic liposomal systems based on photoluminescence imaging and phototherapeutic methodologies.

Author contributions

Siyi Li: Methodology, investigation, writing – original draft. Qinglin Wang: Data curation, investigation. Yingying Ren: Data curation, investigation. Pengfei Zhong: Methodology, investigation. Pengtao Bao: Methodology, investigation. Shanyue Guan: Conceptualization, supervision, writing – review & editing. Xiaochen Qiu: Supervision, writing – review & editing. Xiaozhong Qu: Conceptualization, supervision, writing – original draft, writing – review & editing, funding acquisition.

Conflicts of interest

There are no conflicts to declare.

Acknowledgements

This work was financially supported by the National Natural Science Foundation of China (52273235), the Fundamental Research Funds for the Central Universities, the Youth Innovation Promotion Association of Chinese Academy of Sciences (Grant No. 2019027), Logistic Support Department of CMC Health Care Project (No. 21BJZ35) and Beijing Natural Science Foundation (No. 7212104).

References

- 1 R. C. Wender, O. W. Brawley, S. A. Fedewa, T. Gansler and R. A. Smith, *CA Cancer J. Clin.*, 2019, **69**, 50–79.
- 2 X. Xu, X. Huang, J. Sun, J. Chen, G. Wu, Y. Yao, N. Zhou, S. Wang and L. Sun, *Cyborg Bionic Syst.*, 2022, 9829287.
- 3 Q. Qiu, Y. Wen, H. Dong, A. Shen, X. Zheng, Y. Li and F. Feng, *Biomater. Sci.*, 2019, **7**, 5211–5220.
- 4 H. Liu, L. Chen, C. Xu, Z. Li, H. Zhang, X. Zhang and W. Tan, *Chem. Soc. Rev.*, 2018, **47**, 7140–7180.
- 5 N. Horvat, M. S. Rocha, A. L. Chagas, B. C. Oliveira, M. P. Pacheco, M. A. Binotto, N. M. Ikari, D. C. Paranagua-Vezozzo, H. M. Leao-Filho, J. R. T. Vicentini, M. R. Moreira



- da Silva Filho, M. B. Jatene, F. J. Carrilho and G. G. Cerri, *Am. J. Roentgenol.*, 2018, **211**, 1212–1220.
- 6 A. Walter, P. Paul-Gilloteaux, B. Plochberger, L. Sefc, P. Verkade, J. G. Mannheim, P. Slezak, A. Unterhuber, M. Marchetti-Deschmann, M. Ogris, K. Bühler, D. Fixler, S. H. Geyer, W. J. Weninger, M. Glösmann, S. Handschuh and T. Wanek, *Front. Phys.*, 2020, **8**, 47.
- 7 J. He, C. Li, L. Ding, Y. Huang, X. Yin, J. Zhang, J. Zhang, C. Yao, M. Liang, R. P. Pirraco, J. Chen, Q. Lu, R. Baldrige, Y. Zhang, M. Wu, R. L. Reis and Y. Wang, *Adv. Mater.*, 2019, **31**, 1902409.
- 8 J. D. Mieog, F. B. Achterberg, A. Zlitni, M. Hutteman, J. Burggraaf, R. J. Swijnenburg, S. Gioux and A. L. Vahrmeijer, *Nat. Rev. Clin. Oncol.*, 2022, **19**, 9–22.
- 9 Z. Yuan, L. Gui, J. Zheng, Y. Chen, S. Qu, Y. Shen, F. Wang, M. Er, Y. Gu and H. Chen, *ACS Appl. Mater. Interfaces*, 2018, **10**, 30994–31007.
- 10 L. Wang, S. Guan, Y. Weng, S. Xu, H. Lu, X. Meng and S. Zhou, *ACS Appl. Mater. Interfaces*, 2019, **11**, 6267–6275.
- 11 L. Wang, X. Qu, Y. Zhao, Y. Weng, G. I. N. Waterhouse, H. Yan, S. Guan and S. Zhou, *ACS Appl. Mater. Interfaces*, 2019, **11**, 35228–35237.
- 12 D. Zhao, M. Xu, S. Yang, H. Ma, H. Li, R. Wu, Y. He, S. Wang and X. Liang, *Biomaterials*, 2022, **282**, 121388.
- 13 Y. Cheng, Z. Qu, Q. Jiang, T. Xu, H. Zheng, P. Ye, M. He, Y. Tong, Y. Ma and A. Bao, *Adv. Mater.*, 2023, 2305095.
- 14 X. Zheng, X. Wang, H. Mao, W. Wu, B. Liu and X. Jiang, *Nat. Commun.*, 2015, **6**, 5834–5845.
- 15 A. Anemone, L. Consolino, F. Arena, M. Capozza and D. L. Longo, *Cancer Metastasis Rev.*, 2019, **38**, 25–49.
- 16 C. S. Parkins, M. R. Stratford, M. F. Dennis, M. Stubbs and D. J. Chaplin, *Br. J. Cancer*, 1997, **75**(3), 319–323.
- 17 M. Izci, C. Maksoudian, B. B. Manshian and S. J. Soenen, *Chem. Rev.*, 2021, **121**, 1746–1803.
- 18 X. Zheng, H. Mao, D. Huo, W. Wu, B. Liu and X. Jiang, *Nat. Biomed. Eng.*, 2017, **1**(4), 57–65.
- 19 K. Yang, G. Yu, R. Tian, Z. Zhou, H. Deng, L. Li, Z. Yang, G. Zhang, D. Liu, J. Wei, L. Yue, R. Wang and X. Chen, *Adv. Funct. Mater.*, 2021, **31**, 2008078.
- 20 S. Yang, L. Zhu, Q. Wang, F. Liang, X. Qu, Z. Gan and Z. Yang, *J. Mater. Chem. B*, 2015, **3**, 404–4051.
- 21 C. Zhou, W. X. Zhao, F. T. You, Z. X. Geng and H. S. Peng, *ACS Sens.*, 2019, **4**(4), 984–991.
- 22 D. Yang, S. Guan, Y. Niu, Z. Xie, S. Zhou and X. Qu, *J. Mater. Chem. B*, 2018, **6**, 2315–2322.
- 23 H. Xiang, J. Cheng, X. Ma, X. Zhou and J. J. Chruma, *Chem. Soc. Rev.*, 2013, **42**(14), 6128–6185.
- 24 S. Zhou, L. Jiang, C. Li, H. Mao, C. Jiang, Z. Wang, X. Zheng and X. Jiang, *Adv. Mater.*, 2023, **35**(36), 2212231.
- 25 S. Zhang, H. Chen, L. Wang, X. Qin, B. Jiang, S. Ji, X. Shen and H. Liang, *Angew. Chem., Int. Ed.*, 2022, **61**, e202107076.
- 26 Y. T. Tsai, J. Zhou, H. Weng, J. Shen, L. Tang and W. J. Hu, *Adv. Healthcare Mater.*, 2014, **3**, 221–229.
- 27 Y. Ren, H. Jin, X. Ma, Y. Lu, Z. Shen, J. Deng, G. I. N. Waterhouse, S. Guan, Y. Huang and X. Qu, *Chem. Eng. J.*, 2023, **455**, 140705.
- 28 J. Zhou, L. Rao, G. Yu, T. R. Cook, X. Chen and F. Huang, *Chem. Soc. Rev.*, 2021, **50**, 2839–2891.
- 29 L. Wang, B. Zhang, X. Yang, S. Guo, G. I. N. Waterhouse, G. Song, S. Guan, A. Liu, L. Cheng and S. Zhou, *Bioact. Mater.*, 2023, **20**, 126–136.
- 30 S. Guan, D. Yang, Y. Weng, H. Lu, X. Meng, X. Qu and S. Zhou, *Adv. Healthcare Mater.*, 2018, **7**, 1701123.
- 31 M. Zhao, Q. Zeng, X. Li, D. Xing and T. Zhang, *Nano Res.*, 2022, **15**(1), 716–727.
- 32 Y. Weng, S. Guan, L. Wang, H. Lu, X. Meng, G. I. N. Waterhouse and S. Zhou, *Small*, 2020, **16**, 1905184.
- 33 P. H. D. Nguyen, M. K. Jayasinghe, A. H. Le, B. Peng and M. T. N. Le, *ACS Nano*, 2023, **17**, 5187–5120.
- 34 W. He, X. Xing, X. Wang, D. Wu, W. Wu, J. Guo and S. Mitragotri, *Adv. Funct. Mater.*, 2020, **30**, 1910566.
- 35 C. Liu, H. Chen, H. Zhou, S. Yu, Y. Zhao, N. Wang, W. Yao, A. Lu and W. Qiao, *Appl. Mater. Today*, 2022, **26**, 101368.
- 36 R. C. Van Lehn and A. Alexander-Katz, *ACS Cent. Sci.*, 2017, **3**, 186–195.
- 37 Y. Wang, C. Zhang, K. Yang, Y. Wang, S. Shan, Y. Yan, K. A. Dawson, C. Wang and X. Liang, *Natl. Sci. Rev.*, 2021, **8**(6), 23–33.
- 38 Y. Li, H. Cong, S. Wang, B. Yu and Y. Shen, *Biomater. Sci.*, 2020, **8**, 6442–6468.
- 39 Y. Lu, G. Allegri and J. Huskens, *Mater. Horiz.*, 2022, **9**, 892–907.
- 40 K. Dutta, D. Bochicchio, A. E. Ribbe, D. Alfandari, J. Mager, G. M. Pavan and S. Thayumanavan, *ACS Appl. Mater. Interfaces*, 2019, **11**, 24971–24983.
- 41 J. Gu, W. P. Cheng, J. Liu, S. Y. Lo, D. Smith, X. Qu and Z. Yang, *Biomacromolecules*, 2008, **9**, 255–262.
- 42 C. Ding, J. Gu, X. Qu and Z. Yang, *Bioconjugate Chem.*, 2009, **20**, 1163–1170.
- 43 X. Qu and Z. Yang, *Chem. – Asian J.*, 2016, **11**(19), 2633–2641.
- 44 F. W. Vergeer, X. Chen, F. Lafolet, L. De Cola, H. Fuchs and L. F. Chi, *Adv. Funct. Mater.*, 2006, **16**, 625–632.
- 45 X. Qu, L. Omar, T. B. H. Le, L. Tetley, K. Bolton, K. W. Chooi, W. Wang and I. F. Uchegbu, *Langmuir*, 2008, **24**, 9997–10004.
- 46 C. Zheng, Q. Zhong, W. Song, K. Yi, H. Kong, H. Wang, Y. Tao, M. Li and X. Chen, *Adv. Mater.*, 2023, **35**, 2206989.
- 47 M. Grossi, M. Morgunova, S. Cheung, D. Scholz, E. Conroy, M. Terrile, A. Panarella, J. C. Simpson, W. M. Gallagher and D. F. O'Shea, *Nat. Commun.*, 2016, **7**, 10855.
- 48 Y. Chen, T. Wu, S. Xie, Y. Bai and H. Xing, *Sci. Adv.*, 2023, **9**, 2583–2596.
- 49 S. Fadhel Abbas Albaayit, R. Maharjan, R. Abdullah and M. Hezmee Mohd Noor, *J. Appl. Biomed.*, 2022, **20**(1), 15–21.
- 50 M. Hasan, A. Nishimoto, T. Ohgita, S. Hama, H. Kashida, H. Asanuma and K. Kogure, *J. Controlled Release*, 2016, **228**, 20–25.
- 51 Y. Liu, K. M. Castro Bravo and J. Liu, *Nanoscale Horiz.*, 2021, **6**, 78–94.
- 52 A. M. Wagner, J. M. Knipe, G. Orive and N. A. Peppas, *Acta Biomater.*, 2019, **94**, 44–63.



- 53 A. Wilkinson, E. Lattmann, C. B. Roces, G. K. Pedersen, D. Christensen and Y. Perrie, *J. Controlled Release*, 2018, **291**(10), 1–26.
- 54 D. Witzigmann, J. A. Kulkarni, J. Leung, S. Chen, P. R. Cullis and R. van der Meel, *Adv. Drug Delivery Rev.*, 2020, **159**, 344–363.
- 55 L. Zeng, P. Gupta, Y. Chen, E. Wang, L. Ji, H. Chao and Z. Chen, *Chem. Soc. Rev.*, 2017, **46**(19), 5771–5804.
- 56 W. Sun, M. Parowatkin, W. Steffen, H. J. Butt, V. Mailander and S. Wu, *Adv. Healthcare Mater.*, 2016, **5**, 467–473.

